Neuromechanical wave resonance in jellyfish swimming

Alexander P. Hoover[a,1], Nicole W. Xu[b], Brad J. Gemmell[c], Sean P. Colin[d,e], John H. Costello[e,f], John O. Dabiri[g], and Laura A. Miller[h]

[a]Department of Mathematics, The University of Akron, Akron, OH 44325; [b]Department of Bioengineering, Stanford University, Stanford, CA 94305; [c]Department of Integrative Biology, University of South Florida, Tampa, FL 33620; [d]Marine Biology/Environmental Sciences, Roger Williams University, Bristol, RI 02809; [e]Whitman Center, Marine Biological Laboratory, Woods Hole, MA 02543; [f]Biology Department, Providence College, Providence, RI 02908; [g]Department of Mechanical and Civil Engineering, California Institute of Technology, Pasadena, CA 91125; and [h]Department of Mathematics, University of Arizona, Tucson, AZ 85721

Edited by Leslie Greengard, New York University, New York, NY, and approved January 31, 2021 (received for review September 28, 2020)

For organisms to have robust locomotion, their neuromuscular organization must adapt to constantly changing environments. In jellyfish, swimming robustness emerges when marginal pacemakers fire action potentials throughout the bell's motor nerve net, which signals the musculature to contract. The speed of the muscle activation wave is dictated by the passage times of the action potentials. However, passive elastic material properties also influence the emergent kinematics, with time scales independent of neuromuscular organization. In this multimodal study, we examine the interplay between these two time scales during turning. A three-dimensional computational fluid–structure interaction model of a jellyfish was developed to determine the resulting emergent kinematics, using bidirectional muscular activation waves to actuate the bell rim. Activation wave speeds near the material wave speed yielded successful turns, with a 76-fold difference in turning rate between the best and worst performers. Hyperextension of the margin occurred only at activation wave speeds near the material wave speed, suggesting resonance. This hyperextension resulted in a 34-fold asymmetry in the circulation of the vortex ring between the inside and outside of the turn. Experimental recording of the activation speed confirmed that jellyfish actuate within this range, and flow visualization using particle image velocimetry validated the corresponding fluid dynamics of the numerical model. This suggests that neuromechanical wave resonance plays an important role in the robustness of an organism's locomotory system and presents an undiscovered constraint on the evolution of flexible organisms. Understanding these dynamics is essential for developing actuators in soft body robotics and bioengineered pumps.

jellyfish | propulsion | neuromechanics | fluid–structure interaction | maneuverability

To withstand gusts of wind or unexpected currents, swimming and flying animals must have a level of robustness in their locomotory system to maintain control. This robustness is ingrained in the neuromechanical system, which actuates the trunk and appendages to allow for a set of complex maneuvers, such as predator evasion (1, 2), prey capture (3), and other events involving turning (4–7). For many swimming and flying animals, the emergent kinematics during these maneuvers are a direct result of the interplay between the motor nervous system, musculature, body elasticity, and local fluid environment.

Despite its a relatively simple nervous system (8–11), jellyfish maintain a level of control in a variable fluid environment, from navigating the water column (12, 13) to actively preying on zooplankton (14). Remarkably, the scyphomedusae or "true" jellyfish are able to control their movement using a motor nerve net (MNN), activated by any or all of eight individual pacemakers, which operate without direct communication among one another (15). The pacemakers, spaced equally along the margin of the bell, generate action potentials that propagate throughout the MNN. The action potentials then activate the local swimming muscles, which deform the elastic mesoglea that maintains the bell form.

Previous work has demonstrated the efficiency of jellyfish locomotion, especially for moon jellyfish (*Aurelia* sp.) and other species with oblate bells, compared to swimming fish and crustaceans (16). Their low energetic costs result from advantageous interactions of the starting and stopping vortex rings formed during the contraction and relaxation of the bell, respectively (17–19). This process, known as passive energy recapture, enables the stopping vortex to direct fluid into the bell cavity, which continues to propel the jellyfish forward at no additional metabolic cost (20).

In addition, recent work by Gemmell et al. (21) has demonstrated the fluid dynamics and underlying nerve net activation of turning. To perform a turn, the jellyfish asymmetrically contracts its bell to form an asymmetrical vortex ring. This asymmetry is due to the initial firing of action potentials by pacemakers on the leading edge of the turn (22, 23). The action potentials propagate in both directions along the MNN, away from the pacemaker (10, 24–26). The resulting wave of muscular activation travels along the bell margin, yielding an asymmetrical contraction. Recent studies have incorporated network neural models to demonstrate the passage of action potentials in the MNN (27).

Significance

Despite a relatively simple nervous system, jellyfish manage a broad range of motion from a distributed set of pacemakers, which initiate action potentials that form a wave of muscular activation to drive the bell motion. In this interdisciplinary study, we find that successful turning maneuvers are dependent on the speed of this activation wave. Using a three-dimensional computational fluid–structure interaction model, we demonstrate that setting the activation wave speed near the bell's material wave speed, from the elastic wave equation, yields the strongest turning and margin hyperextension. This suggests an undescribed neuromechanical constraint on the bell, an important finding pertinent to the actuation of biomimetic vehicles and tissue-engineered pumps, as well as the biology of locomotion in flexible animals.

Author contributions: A.P.H., N.W.X., B.J.G., S.P.C., J.H.C., J.O.D., and L.A.M. designed research; A.P.H., N.W.X., B.J.G., S.P.C., and J.H.C. performed research; A.P.H., N.W.X., B.J.G., S.P.C., J.H.C., J.O.D., and L.A.M. analyzed data; and A.P.H., N.W.X., and L.A.M. wrote the paper.

The authors declare no competing interest.

This article is a PNAS Direct Submission.

[1]To whom correspondence may be addressed. Email: ahoover1@uakron.edu.

This article contains supporting information online at https://www.pnas.org/lookup/suppl/doi:10.1073/pnas.2020025118/-/DCSupplemental.

Published March 8, 2021.

Table 1. Comparison of the theoretical material wave speed and the FSI model's recorded wave speed

Young's modulus	$\frac{1}{4}\nu_{ref}$	ν_{ref}	$4\nu_{ref}$
Theoretical wave speed c_t (m/s)	0.15811	0.31623	0.63246
Recorded model wave speed, c_r (m/s)	0.15906	0.32221	0.66139

Little is known about the interaction between the temporal dynamics of the MNN and the time scales associated with the elastic response of the mesoglea. Previous experiments found that certain jellyfish swimming gaits resulted from resonant driving by the animal actuating its bell at the natural frequency (28–30). Subsequent computational fluid dynamics studies confirmed that driving the bell at its period of free vibration yields peak swimming speeds (31, 32). For these studies, the time scale associated with the mesoglea is that of the bell's period of free vibration.

However, the mesoglea itself is also an elastic material with an internal material wave speed. As action potentials travel around the MNN, the coronal swimming muscles activate and locally deform the mesoglea. Treating the bell as a deformable elastic domain, the local deformations of the mesoglea, in turn, produce a circumferential wave of elastic deformation that propagates to other regions of the mesoglea. The speed of the elastic wave is thus dependent on the stiffness and density of the material (33). Resonance in the context of these neuromechanical waves embedded in an elastic medium has not been fully explored but is crucial in understanding the evolutionary constraints and control mechanisms of jellyfish and other soft-body invertebrates.

Furthermore, the proliferation of soft robotics (34–37) and tissue-engineered pumps (38, 39) presents new challenges related to this paradigm. Embedding actuators in soft materials compels a deeper understanding of the interplay between the temporal dynamics of the actuators and the material's local response. Elucidating how such dynamics govern the neuromechanical systems of soft-body invertebrates such as jellyfish can in turn aid in the design of these devices.

In this study, we have quantified the interplay between the speed of actuation and the material's elastic response by examining both roles in the turning mechanisms of scyphozoan jellyfish. This was done by using a combination of computational fluid dynamics and experiments with live *Aurelia aurita*. The model results were validated by comparing the recordings of kinematics from induced muscular activation waves and flow-field digital particle image velocimetry (DPIV).

Results

Numerical simulations were performed using a fully coupled fluid–structure interaction (FSI) model of an elastic bell body in a viscous fluid. To simulate this problem, we used a hybrid immersed boundary/finite element framework (40–42) that has been applied to a variety of biological FSI problems (43–46). The hemiellipsoid jellyfish bell model that is used in this study was previously validated in forward-swimming studies (32, 47).

In this FSI model, the kinematics were not prescribed, and the bell was driven with an applied active tension that models the action of the muscle. The resulting deformations and fluid motion emerged as a result of the interplay between the passive elastic properties, active muscle model, and local fluid environment. The bell elastic properties are described within a continuum mechanics framework, in which the mesoglea was modeled as a neo-Hookean material with uniform elastic modulus, ν. The muscles were modeled using a time-dependent circumferential stress applied along the bell margin, with magnitude proportional to the bell stiffness to ensure the same amount of bell deformation (see *SI Appendix*, *Methods* for more details).

Two sets of simulation were performed. In the first set of simulations, the bell was deformed to determine the material wave speed in the circumferential direction. In the second set of simulations, turning was performed by applying a traveling wave of active tension along the margin of the bell to model the action of the swimming muscles. Additional details are as follows.

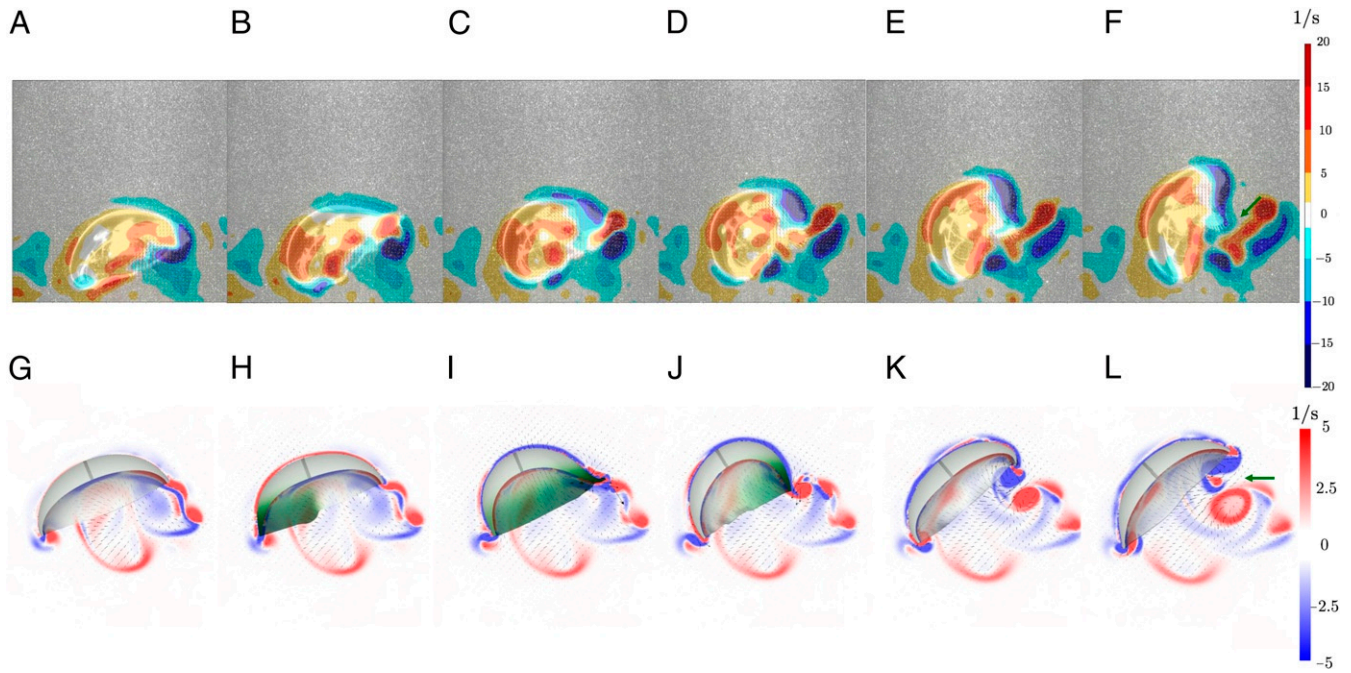

Fig. 1. (*A–F*) DPIV frames of the vorticity of an *Aurelia* sp. executing a turn. (*G–L*) Snapshots of the model bell ($\nu = \nu_{ref}$, $\tau = 10^{-0.4}$ s) and the out-of-plane vorticity generated by a second wave of active tension at times 2.0 s (*G*), 2.2 s (*H*), 2.375 s (*I*), 2.5 s (*J*), 2.75 s (*K*), and 3.0 s (*L*). The bell color indicates the instantaneous strength of contraction, in which dark green indicates the presence of tension and white is the absence of tension.

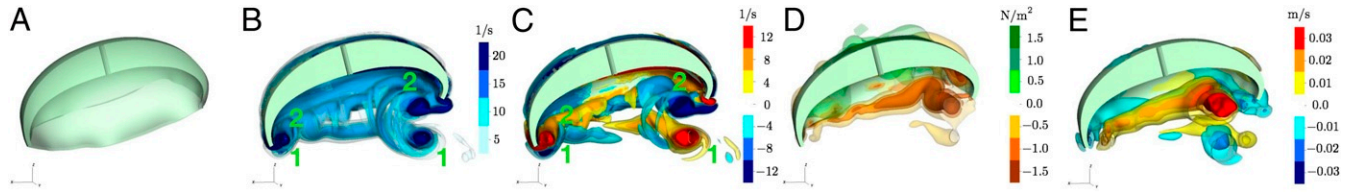

Fig. 2. Half-plane plot lots of the bell model's mesh at time 0.75 s (*A*), along with isocontours of the vorticity magnitude (s^{-1}) (*B*), *y* component of vorticity (s^{-1}) (*C*), pressure (N/m^2) (*D*), and the vertical velocity (m/s) (*E*). The starting and stopping vortex rings are labeled 1 and 2, respectively, in *B* and *C*. The isocontours are symmetric across the *xz* plane.

Additionally two sets of experiments were performed. DPIV measurements of *Aurelia* sp. were taken as the jellyfish was performing multiple turning maneuvers, revealing the underlying fluid dynamics (*Materials and Methods*). Experimental measurements of wave speeds were calculated in live *A. aurita* medusae by tracking the contractile motion of the bell in $n = 6$ cases, using the time delays and arc lengths between two visible implant elastomer (VIE) tags.

Comparison of the Theoretical, Computational, and Recorded Material Wave Speed. To compare the numerical model's material wave speed with the theoretical elastic wave speed from the elastic wave equation, numerical experiments were performed to determine the wave speed in our FSI model. The application of the stress deforms the region where the stress is applied and creates a wave of elastic deformation that travels along the margin of the bell mesoglea (Movie S1). In general, the wave speed of an undamped material is $c_t = \sqrt{\nu/\rho_m}$, where ρ_m is the effective density of the material. As an estimate, we assume that a neutrally buoyant jellyfish has the same density of the fluid, and we can approximate how the wave speed scales with changes in the elastic modulus.

Because the material wave speed of the bell is a root function of the bell stiffness, to halve or double the material wave speed of a bell, the stiffness must be a quarter or quadruple the reference bell stiffness, respectively. To characterize the wave speed associated with the bell FSI model with a uniform elastic modulus, ν, a uniform stress was applied and sustained on a region corresponding to one-eighth of the bell margin. The passage time of the elastic wave deformation to reach the other side of the bell, τ_r, is recorded for three bells of differing elastic moduli $\nu = \frac{1}{4}\nu_{ref}, \nu_{ref}$, and $4\nu_{ref}$, where $\nu_{ref} = 100$ Pa (Movie S2). The wave speed of the bell is then calculated with respect to τ_r and half the bell diameter, $c_r = r \cdot \pi/\tau_r$ m/s ($r = 0.02$ m). Comparing the model's recorded wave speed, c_r, with the theoretical wave speed, c_t, we find close agreement (<5% difference) between the two values (Table 1).

To compare, the mean and SD of the experimentally measured muscle wave speed in live *A. aurita* was 0.474 ± 0.132 m/s, with a range from 0.319 to 0.672 m/s using $n = 6$ cases (two at 0.25 Hz, two at 0.50 Hz, and two at 1.00 Hz). The experimental contractile speeds reside within the range of observed values in literature, with previous mean speeds of 0.4 to 0.5 m/s and a large spread from 0.22 to 1.00 m/s, including in animals with pacemakers excised to prevent multiple pacemakers from activating contractions along the muscle ring (22, 48, 49). Although previous work suggests that the strength of mechanical stimuli affects contractile speeds, the muscle wave speeds observed in this study were not dependent on the frequency of electrical stimulation. The highest contractile speed occurred at 0.25 Hz, and the two slowest speeds occurred at 0.50 and 1.00 Hz.

Actuating the Bell at the Natural Wave Speed Yields Resonant Behavior. During turning maneuvers, one pacemaker dominates the neural activity of the bell (8, 15, 21, 22). This effectively produces a bidirectional wave of action potentials originating from the site of the firing pacemaker (10, 23). These action potentials travel through the MNN and meet at the opposite side of the bell, where the refractory period of the neurons do not allow the waves to continue. This neural activity yields an asymmetric contraction of the bell that follows the path of the action potential waves. To simulate this phenomenon, the bell model was

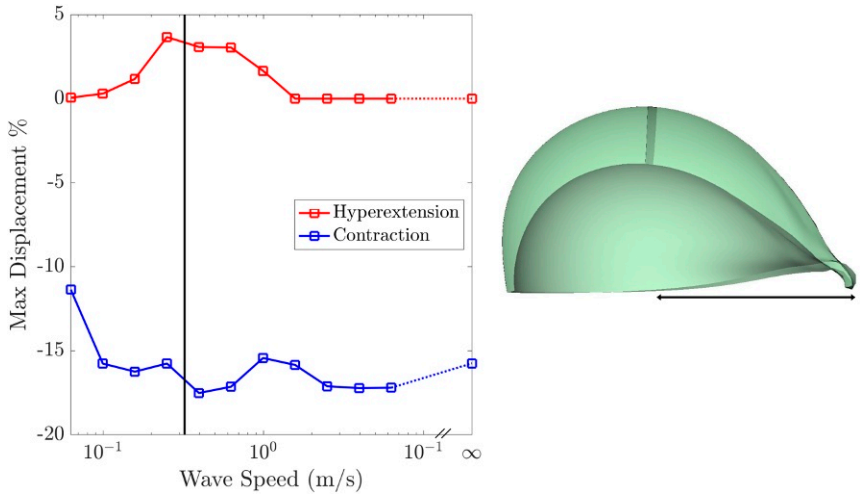

Fig. 3. (*Left*) Plot of the percentage of hyperextension (red) and contraction (blue) of the bell margin on the outside of the turn for differing activation wave speeds. Note that the bell margin only hyperextends for activation wave speeds near the material wave speed (black). (*Right*) A diagram displaying how the hyperextension of the bell margin is measured.

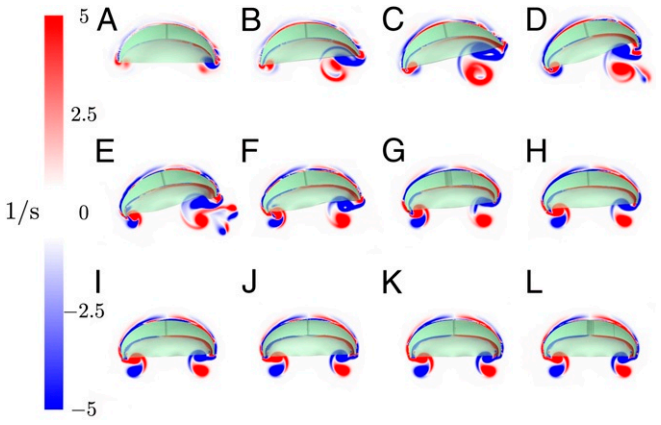

Fig. 4. Plots of the out-of-plane vorticity 0.5 s after the passage of the activation wave for different runs where $c_a = r \cdot \pi/10^{0.0}$ m/s (*A*), $r \cdot \pi/10^{-0.2}$ m/s (*B*), $r \cdot \pi/10^{-0.4}$ m/s (*C*), $r \cdot \pi/10^{-0.6}$ m/s (*D*), $r \cdot \pi/10^{-0.8}$ m/s (*E*), $r \cdot \pi/10^{-1.0}$ (*F*), $r \cdot \pi/10^{-1.2}$ m/s (*G*), $r \cdot \pi/10^{-1.4}$ m/s (*H*), $10^{-1.6}$ m/s (*I*), $r \cdot \pi/10^{-1.8}$ m/s (*J*), $r \cdot \pi/10^{-2.0}$ m/s (*K*), and 0.0 m/s (*L*). The bell is initially at rest in quiescent flow.

actuated using a bidirectional wave of applied tension with a fixed wave speed (Movies S3 and S4). The activation and duration of applied tension is held constant for each case considered. The passage time for the wave of muscle activation to travel from one side of the bell to the other, τ, is varied across a set of simulations, where $\tau = 10^{-k}$ s for $k = 0.0$ to 2.0 in 0.2 increments. This passage time corresponds to the activation wave speed, $c_a = r \cdot \pi/\tau$, and we will refer to the latter for the studies that follow.

Model measurements of jellyfish turning were remarkably similar to observed experimental turns when the muscle activation wave speed, c_a, is near the material wave speed, c_r. Fig. 1 compares the vorticity and activation wave generated by the bell model near the material wave speed to DPIV frames generated by a turning moon jellyfish (*Aurelia* sp.). The DPIV frames illustrate a jellyfish executing multiple turns over consecutive contraction cycles, while the simulation results show the resulting flow field of the jellyfish performing a turning maneuver based on our model. For the purposes of comparison, the simulation results are shown for a second turning maneuver (Movie S5). Initially (Fig. 1 *A* and *G*), both the moon jellyfish bell and the model bell are in a fully relaxed state, with vorticity of the previous turn still present. At the start of the turn (Fig. 1 *B* and *H*), the bell margin on the inside of the turn contracts as the activation wave travels along the bell margin circumferentially. As the wave of actuation travels around the bell, the margin on the outside of the turn begins to hyperextend and contract (Fig. 1 *C*, *D*, *H*, and *J*). The muscular activation and the elastic response to the hyperextension cause the bell margin to be pulled in toward the central axis of the bell. This movement then produces a strong flow pattern in the interior of the bell that pulls fluid from the hyperextended bell margin toward the bell's central axis. As the wave of actuation abets (Fig. 1 *E* and *K*), the bell margin expands back to its original position, generating a stopping vortex ring that rotates in the opposite direction of the starting vortex generated during the contraction. The interaction of the starting and stopping vortex on the outside of the turn directs fluid flow to the interior cavity (Fig. 1 *F* and *L*), while the absence of a strong starting and stopping vortex on the inside of the turn yields a lower refilling flow on the inside of the turn. This flow pattern in the subumbrellar cavity on the outside edge continues to turn the bell after muscular activity has ceased (Fig. 1*F*). Differences are present when comparing the starting vortex ring on the inside of the turn, which can be attributed to the additional control mechanisms from the radial musculature (21), but the overall motion of the bell model is very similar to that of the organism. This comparison suggests the model's resulting fluid dynamics are in accordance with the experimental DPIV results of the organism turning.

As the activation wave travels along the bell rim, the elastic potential energy and momentum increase with the wave. Once the activation wave reaches the other end of the bell, the potential energy is released and allows for the hyperextension and elastic recoil that form the counter-rotating vortex rings. During the contraction and hyperextension of the bell margin, the motion of the margin forms the starting vortex ring. The stopping vortex ring is formed after the contraction due to the elastic recoil of the margin and the bell's subsequent expansion. In Fig. 2, we have plotted the mesh and isocontours of fluid properties after the expansion of the bell (time = 0.75 s). The resulting fluid dynamics are symmetric across the xz plane, such that the bell's center of mass of maintains the same y coordinate throughout the simulation. Examining the vorticity magnitude (Fig. 2*B*), we note the presence of two asymmetrical vortex rings, with a large region of vorticity formed on the outside of the turn (see also Movie S6). This asymmetry is due to the lack of a buildup in momentum and elastic recoil as a consequence of the passage of the activation wave. This is further illustrated with the isocontours of the y component of vorticity (Fig. 2*C*), where we note the counter-rotation of the starting and stopping vortex ring. Negative pressure isocontours (Fig. 2*D*) in the bell cavity on the outside of the turn, suggesting a region of suction that would allow the bell to pull itself through the fluid and continue turning (50, 51). The isocontours of the vertical velocity are included (Fig. 2*E*) to highlight how the interaction between the asymmetric starting and stopping vortex rings direct fluid in the bell.

A similar flow pattern is observed for straight swimming jellyfish, as a stopping vortex ring is generated during bell expansion. The stopping vortex ring continues to direct fluid flow into the bell, providing a secondary source of thrust known as passive energy recapture (16). Whereas the forward-swimming jellyfish stopping vortex ring is fairly uniform during forward swimming,

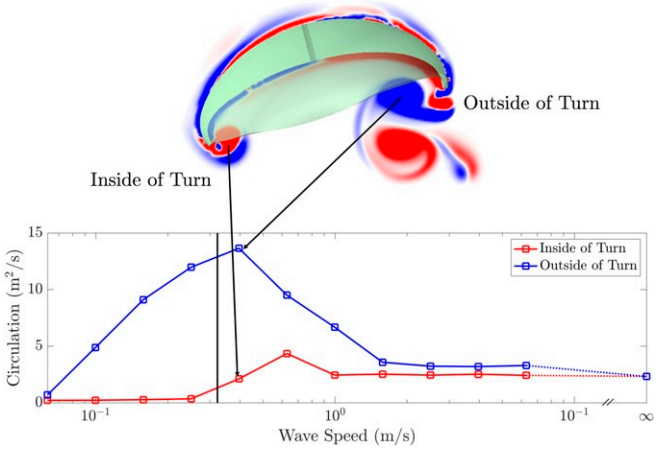

Fig. 5. Plot comparing the circulation of the inside (red) and outside (blue) of the turn 0.5 s after the passage of the wave of muscular activation for various activation wave speeds, with the material wave speed, c_r, noted in black. We observe that the circulation generated on the outside of the turn increases as the activation wave speed approaches the material wave speed, peaking at a speed slightly higher than that of the material wave speed. The circulation found on the inside of the turn is initially minimal, but then grows for $c_a \geq r \cdot \pi/r \cdot \pi 10^{-0.8}$ before plateauing. At faster activation wave speeds, the circulation between the inside and outside of the turn begin to converge, as would be expected for a uniform activation of the bell.

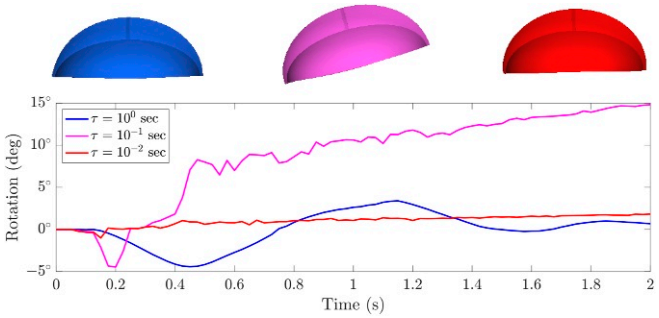

Fig. 6. Plot comparing the turn angle along the central axis of the bell ($\nu = \nu_{ref}$) for three wave speeds, $c_a = r \cdot \pi/10^0$, $r \cdot \pi/10^{-1}$, and $r \cdot \pi/10^{-2}$ m/s. We note that the activation wave speed corresponding to the closest to the material wave speed, $c_a = r \cdot \pi/10^{-1}$ m/s, yields a significant turn. We also note that the bell in this case continues to turn long after the activation wave due to the vortex dynamics shown in Fig. 4.

we find that the uniformity of the stopping vortex ring is dependent on the wave speed and the resulting hyperextension of the bell margin at the outside of the turn. For wave speeds that were slower than the material wave speed, the hyperextension of the bell is minimal (Fig. 3), and the resulting vorticity present on the outside of the turn is similar to that of the inside of the turn (Fig. 4), although both are weak and yield little motion. The motion of the bell on the inside of the turn produces vorticity that is counter-rotating with respect to the motion of the outside of the turn. As the activation wave speed approaches that of the material wave speed, the hyperextension increases and yields a larger region of vorticity relative to the inside of the turn. As the wave speed increases further, the discrepancy in the vorticity between the inside and outside of the turn decreases, which yields a bell that resembles the symmetric vortex ring produced during forward swimming (Fig. 4*L*). We note that a uniformly actuated bell is equivalent to the case of an infinite wave speed. Furthermore, the hyperextension of the bell margin is not present for higher wave speeds, although the displacement during the contraction is comparable to that of the activation wave speeds closer to the material wave speed. The resulting hyperextension when driving the bell at its material wave speed suggests that the bell is exhibiting resonant behavior due to the large circumferential deformations.

Circulation Analysis Reveals Maximum Vortex Ring Asymmetry When Driven Near the Material Wave Speed. Calculating the circulation (*SI Appendix*, *Materials* and *Methods*) of the stopping vortex ring on the inside and outside of the turn 0.5 s after the activation wave reaches the opposite side of the bell, we find that the asymmetry in the strength of vorticity between the two regions is dependent on the wave speed, as shown in Fig. 5. The slower activation wave speeds produce minimal circulation on both sides of the bell. As the speed increases and approaches the bell's material wave speed, the circulation generated on the outside of the turn, where the hyperextension occurs, grows while the circulation generated on the inside of the turn is minimal. As the activation wave speed increases beyond the material wave speed, the circulation associated with the inside of the turn increases. As the wave speed further increases, the circulation associated with the outside of the turn decreases and approaches the circulation measured on the inside of the turn. Note that the vortex structure present is nearly symmetric, similar to the stopping vortex ring generated during forward swimming.

Stronger Rotation Occurs When Driving Near the Material Wave Speed. Significant differences occur when varying the wave speed over a logarithmic scale. In Fig. 6, the rotation of the central axis of the bell over time for the activation wave speeds of $c_a = r \cdot \pi/10^0$, $r \cdot \pi/10^{-1}$, and $r \cdot \pi/10^{-2}$ m/s (Movie S7). The wave speed closest to the material wave speed, $c_a = r \cdot \pi/10^{-1}$ m/s, yields a significant rotation that continues over time. Furthermore, we find that the bell has a sustained period of positive radial velocity due to the presence of strong vorticity on the outside of the turn, as noted in Figs. 4 and 5. The faster wave speed yields little rotation of the bell during the passage of the activation wave but moved the bell forward due to the vortex ring generated. The slower wave speed yielded a rotation of the central axis during the passage of the activation wave. However, the material response following the end of the activation wave reversed the resulting rotation, and the vortex structures generated did not turn the bell.

Varying Material Properties Alter the Optimal Turning Wave Speed. Varying the material properties of the bell affected the optimal wave speed for turning. By examining the cases where the elastic modulus was a quarter and four times that of the reference case, such that $\nu = 1/4\nu_{ref}$ and $4\nu_{ref}$, we effectively halved and doubled the material wave speed of the bell, respectively. The activation wave speed was again varied for the stiffer and more flexible bell (Movie S8). In Fig. 7, the turn angle formed by the inside and outside of the bell after 2 s was recorded. The wave speeds associated with the strongest turn correspond to the material wave speed of each bell stiffness. Note that the magnitude of tension applied to the bell is held in proportion to the bell's elastic modulus, which has been shown to yield similar radial deformations in the bell in previous forward-swimming studies (32, 47). Furthermore, varying the bell stiffness and tension in proportion to one another affected the strength of the vorticity generated by the bell, such that increasing the bell elasticity yields stronger vortex rings (47). This effect explains the differences in the turning rate of the bell between the three different cases, in which a stiffer bell produced a stronger region of vorticity on the outside of the turn than a more flexible bell. In all cases, the rate of turning peaked when the activation wave speed matched the material wave speed.

Multiple Activation Waves Increase the Turning Rate. Repeating the activation wave over a 2-s cycle revealed continued turning for each application of the activation wave. Fig. 8 shows the turn angles at the end of the first six cycles for a bell with an activation wave speed of near the material wave speed ($c_a = r \cdot \pi/10^{-0.8}$ m/s). We find a fairly consistent turning angle for each pulsing cycle that average to $41.4°$, with an elevated turn rate for later cycles. This suggests that this is a robust turning mechanism that is regulated by the pacemaker activity.

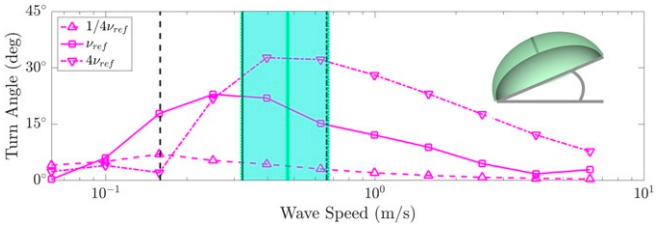

Fig. 7. Plot comparing the resulting turn angle of three bells with $\nu = 1/4\nu_{ref}$ (dashed), ν_{ref} (solid), and $4\nu_{ref}$ (dotted), at 2 s for differing activation wave speeds. We note that the peak turn angle is near the associated material wave speed (plotted in black). This suggests that this turning mechanism is strongly dependent on the interaction between the material properties of the bell and the speed of neuromuscular activation. Shaded in green is the range of speeds observed in *A. aurita*, with the solid green line representing the mean wave speed recorded.

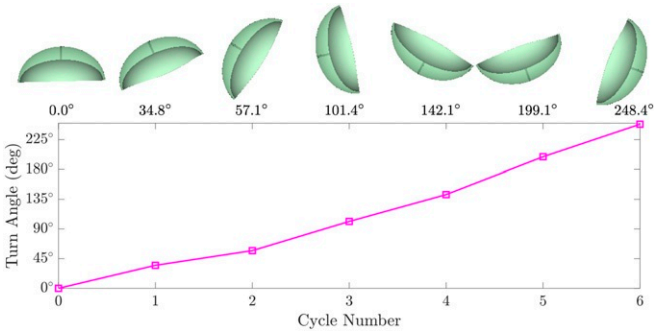

Fig. 8. Plot of the turn angle relative to the center axis of the bell in subsequent 2-s activation cycles for the activation wave speed near the material wave speed, $c_a = r \cdot \pi / 10^{-0.6}$ m/s. We note that the bell continues to consistently turn with each application of the activation wave, which suggests a robust a turning mechanism.

Discussion

In this study, we used a combination of computational and experimental methods to understand the interaction of the elastic properties of a jellyfish bell with the neuromechanical activation of the musculature. In doing so, we demonstrate elastic wave resonance, which occurs when the muscular activation wave speed is near the material wave speed of an elastic material. This elastic material wave speed is proportional to the square root of the elastic modulus of the bell over its density. Using computational FSI methods, we showed that the amount of turning per pulse depends on the activation wave speed relative to the material wave speed. We find good qualitative agreement between the bell deformations and resulting flow fields generated by our numerical jellyfish and the moon jellyfish *Aurelia* sp. (Fig. 1). Furthermore, recorded activation muscle wave speeds from *Aurelia* sp. confirm that the range of speeds observed are within the range of activation wave speeds that execute efficient turning in the computational model (Fig. 7).

The results of this study suggest a strong neuromechanical evolutionary constraint on the flexibility of the bell margin, muscle activation dynamics, and neural organization. Scyphozoan jellyfish rely on the MNN to activate their musculature, with local muscle contractions triggered by the passage of action potentials through the nerve net. The action potentials originate from a set of symmetrically distributed pacemakers in the rhopalia of the bell. The only direct line of communication between one pacemaker to another is via the MNN, unlike the nerve rings and

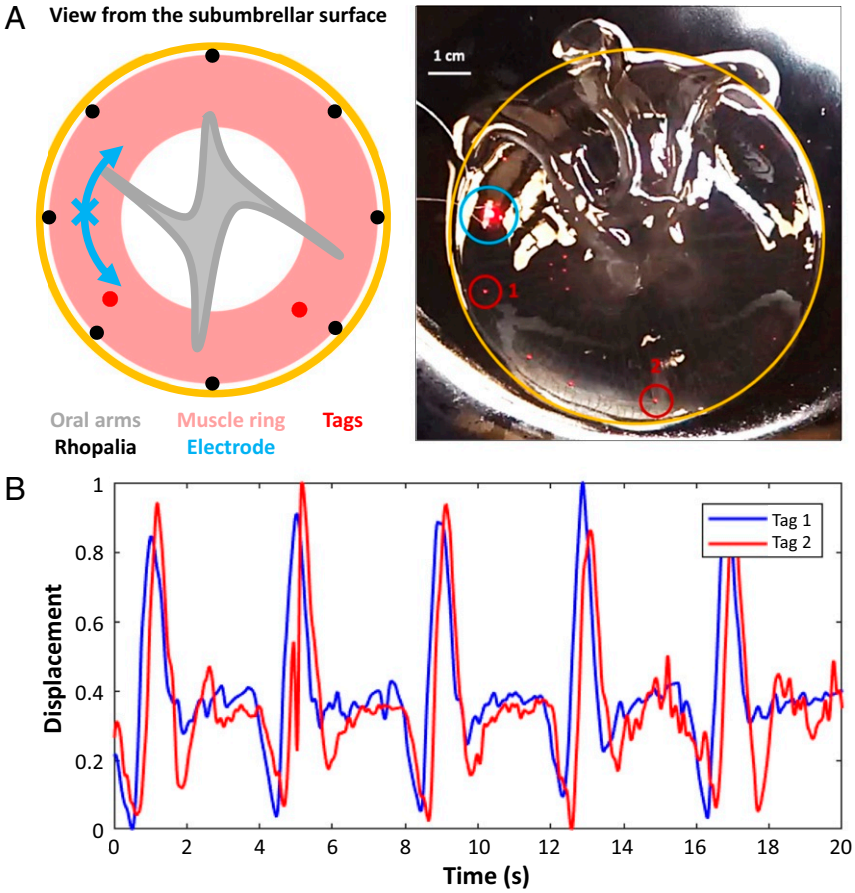

Fig. 9. Experiments to measure jellyfish muscle contractile speeds. (*A*) To calculate experimental muscle wave speeds, muscle contractions of jellyfish were recorded using movies taken at 60 fps. (*A*, *Left*) A schematic of the jellyfish bell, with labels for the oral arms, rhopalia, muscle ring, electrode with arrows showing the bidirectional muscle wave propagation, and injected tags. (*A*, *Right*) A representative frame for one animal (diameter of 8.5 cm). The raw image includes reflections of light from the transparent mesoglea and black plate. The jellyfish (bell outlined in yellow) was placed subumbrellar surface upward on a black dish in the absence of water. An electrode (circled in blue) was embedded into the tissue, with a red light-emitting diode shown for visual confirmation of the electrical signal. Red tags were injected into the marginal tissue (two tags circled in red). The circled tags, labeled 1 and 2, were tracked to obtain displacement curves, as shown in one example displacement curve in *B*, in which one animal was driven at 0.25 Hz. The time delay between the two tags was used to calculate the muscle wave-propagation speed. Additional displacements are illustrated in *SI Appendix*, Fig. S2.

coordinated muscular activity found in Hydrozoan jellyfish (8). Even with the relatively simple nature of this distributed control mechanism, jellyfish manage to perform complicated maneuvers (21, 27). Ultimately, the turn was initiated by a temporal mismatch in the contraction of opposite sides of the bell by controlling propagation of muscle contraction around bell. However, the results of this study show that the robustness of the locomotory system is only possible if the flexibility of the bell margin is tuned to the speed of the activation wave generated by the neural system. Similar observations had been found previously by the authors in the case of forward swimming when the frequency of coronal muscle contraction is tuned to the frequency of free vibration when the bell is squeezed and released (32). This is further aided by the presence of the weaker radial musculature, which helps direct the kinematics of the edge of the bell margin on the inside of the turn (21).

This study provides evidence of neuromechanical wave resonance as having a significant role for the performance in turning and maneuvering. Using the theoretical wave speed of the material, we are able to show that if the activation wave speed is significantly above and below the material wave speed, the larger displacements of the bell margin necessary for turning cannot be generated. To illustrate, when examining the hyperextension of the bell margin on the outside of the turn, as has been observed experimentally (52), activation wave speeds above and below the material wave speed do not generate bell margin hyperextension (Fig. 3). For slower speeds, the activation wave has a damped elastic response and does not generate the rotational momentum in the wake required to turn (Fig. 5). For faster speeds, the activation wave moves too quickly for the material to respond, yielding vortex dynamics that resemble forward swimmers (Fig. 4). This provides strong evidence of a neuromechanical constraint that is important for a wide range of soft-body fluid–structure systems. Further research into the interplay between elastic wave harmonics and active muscular tension could yield similar insights as those found for undulatory swimmers with Euler–Bernoulli beam-mode analysis (53).

As soft robotics and biomimetic materials become more prevalent in engineering applications (36, 54, 55), understanding the interplay between the material properties of these devices and the timing of the actuating mechanism will be essential for controlling their motion. Jellyfish themselves have inspired biomimetic drones (34, 56, 57) and tissue-engineered pumps (38). The general results of this study can aid the design of future biomimetic pumps, allowing for control principles to be tuned to the take advantage of wave resonance, which can improve the robustness of autonomous submersible propulsion.

Materials and Methods

Immersed Boundary. The immersed boundary method (58) is an FSI framework for coupling the structural dynamics of the immersed bodies in a viscous, incompressible fluid. This is done by coupling the forces acting on the immersed body to a force term in the Navier–Stokes equations. This coupling is performed using a Dirac delta function integral that spreads the forces from the structure to the region of local to the structure. Once the forces acting on the fluid are calculated, the Navier–Stokes equations are solved on a finite difference grid for a fixed domain. The fluid grid is updated using a numerical solver. The coupling is completed by updating the motion of the body by using a Dirac delta function integral on the local fluid grid to interpolate the displacement of the body and maintain a no-slip boundary condition. In this study, the structure is described with a finite element description of the body, using a continuum mechanical description of the elastic energy and material properties of the structure, and a finite difference discretization for the fluid (42). To reduce the computational cost of this three-dimensional simulation while still accounting for the boundary layers and vortex shedding, an adaptive, parallel implementation of the immersed boundary method is used (59). More information on the methods used in this study can be found in *SI Appendix, Methods*.

The computational jellyfish is 4 cm in diameter and is initially centered in a cubic computational domain with sides of length $L = 30$ cm. The boundary conditions are periodic. The adaptive method uses five levels of grid refinement, with the most refined level ($\Delta x = L/1024$) used for regions enclosing the immersed body and where the vorticity magnitude is above a certain threshold. Convergence studies for half and twice the finest level of refinement were performed for a forward-swimming jellyfish, and it was determined that the resulting swimming speed was nearly indistinguishable ($< 2\%$) from the finer level of refinement.

Material Model. The bell's body forces are calculated from the first Piola–Kirchoff stress tensor. The bell's passive material properties, such as the elasticity of the bell, are described using a neo-Hookean material model. The elastic modulus is uniform throughout the bell and chosen to be in line with the rheological measurements of a moon jellyfish mesoglea ($\nu_{ref} = 100$ Pa) (60). The active material properties, which entail the muscular activation, are described by prescribing tension in a fiber direction that mimics the coronally oriented, subumbrellar musculature. The region and duration of muscular activation were informed by experiments (8, 23) and have been validated in previous studies (32, 47). The activation wave is prescribed by implementing a symmetric phase delay of the actuation based on the polar coordinates of a horizontal slice of the bell. More information on the material model used in this study can be found in *SI Appendix, Materials*.

Body Wave Measurements. Muscle wave speeds were calculated by tracking the contractile bell motion of jellyfish medusae, at room temperature (21°C). *A. aurita* (n = 5; diameters from 8.2 to 11.1 cm) were placed subumbrellar surface upward on a plate and injected with red VIE tags (Northwest Marine Technology) along the bell margin (circled in red in Fig. 9). Wire electrodes were embedded into the tissue (circled in blue in Fig. 9*A*) to generate pulses at 0.25, 0.50, and 1.00 Hz using a MyoPacer Cell Stimulator (IonOptix), as described previously by Xu and Dabiri (61). Stimulated muscle contractions originated at the electrode location and propagated bidirectionally outward, removing the occurrence of multiple swim pacemakers firing simultaneously, as observed in natural jellyfish muscle contractions.

Movies were recorded at 60 fps on a Cyber-shot DSC-RX100 (Sony Corporation of America). Centroids of two tags (labeled 1 and 2 in a representative image; Fig. 9*A*) were tracked to obtain the displacement, relative to a reference image in which the tag was stationary during a latent or relaxed phase of jellyfish locomotion. The displacements (a representative example shown in Fig. 9*B*) were calculated by smoothing and subtracting a moving average of 1.67 s from the total displacement, to reduce bulk motion of the bell in the plate. The arc length was calculated by using the jellyfish diameter and angle between the two tags. The time delay was obtained by determining the lag for the largest absolute value of the normalized cross-correlation between the two tag displacements over 20 s, implemented using the MATLAB function "finddelay." Wave speeds were calculated using the arc length and lag time.

Particle Image Velocimetry. We used high-speed DPIV to obtain resulting flow fields around the jellyfish. Recordings were acquired by a high-speed digital video camera (Fastcam 1024 PCI; Photron) at 1,000 frames per second (1024 × 1024 pixels) with a scale factor 0.178 mm per pixel. Seeding particles (10-mm hollow glass beads; Potters Industries) were illuminated by two laser sheets (532 nm, 600 mW continuous wave) mounted in the same plane on opposite sides of the tank to eliminate shadows on either side of the tank as each animal swam within the field of view. Medusae of juvenile *A. aurita* (2 to 6 cm) were obtained from the New England Aquarium and maintained at 25 °C in 20-L aquaria. Animals were recorded while freely swimming in a 30 × 10 × 25 cm glass vessel, using a method reported previously (16).

Fluid velocity vectors were determined from sequential images analyzed using a cross-correlation algorithm (LaVision software). Image pairs were analyzed with shifting overlapping interrogation windows of a decreasing size of 32 × 32 pixels to 16 × 16 pixels.

Data Availability. All study data are included in the article, *SI Appendix*, and Movies S1–S8.

ACKNOWLEDGMENTS. We thank Cabrillo Marine Aquarium for providing *A. aurita* for experimental muscle wave speed calculations. We also thank Boyce Griffith for assistance regarding model implementation. This research was funded by the NSF Division of Mathematical Sciences, under Faculty Early Career Development Program Grant 1151478 (to L.A.M.).

1. W. J. Stewart, G. S. Cardenas, M. J. McHenry, Zebrafish larvae evade predators by sensing water flow. *J. Exp. Biol.* **216**, 388–398 (2013).
2. G. O. Mackie, Central neural circuitry in the jellyfish Aglantha: A model 'simple nervous system'. *Neurosignals* **13**, 5–19 (2004).
3. R. Olberg, A. Worthington, K. Venator, Prey pursuit and interception in dragonflies. *J. Comp. Physiol.* **186**, 155–162 (2000).
4. E. Drucker, G. Lauder, Wake dynamics and fluid forces of turning maneuvers in sunfish. *J. Exp. Biol.* **204**, 431–442 (2001).
5. F. T. Muijres, M. J. Elzinga, J. M. Melis, M. H. Dickinson, Flies evade looming targets by executing rapid visually directed banked turns. *Science* **344**, 172–177 (2014).
6. A. J. Bergou, L. Ristroph, J. Guckenheimer, I. Cohen, Z. J. Wang, Fruit flies modulate passive wing pitching to generate in-flight turns. *Phys. Rev. Lett.* **104**, 148101 (2010).
7. B. P. Epps, A. H. Techet, Impulse generated during unsteady maneuvering of swimming fish. *Exp. Fluids* **43**, 691–700 (2007).
8. R. A. Satterlie, Neuronal control of swimming in jellyfish: A comparative story. *Can. J. Zool.* **80**, 1654–1669 (2002).
9. R. A. Satterlie, Do jellyfish have central nervous systems?*J. Exp. Biol.* **214**, 1215–1223 (2011).
10. G. Horridge, The nerves and muscles of medusae. I. Conduction in the nervous system of Aurellia aurita Lamarck. *J. Exp. Biol.* **31**, 594–600 (1954).
11. G. J. Romanes, Further observations on the locomotor system of medusae. *Phil. Trans. Roy. Soc. Lond.* **167**, 659–752 (1877).
12. D. J. Albert, Aurelia labiata medusae (scyphozoa) in Roscoe Bay avoid tidal dispersion by vertical migration. *J. Sea Res.* **57**, 281–287 (2007).
13. D. J. Albert, What's on the mind of a jellyfish? A review of behavioral observations on Aurelia sp. jellyfish. *Neurosci. Biobehav. Rev.* **35**, 474–482 (2011).
14. J. E. Purcell, Predation by Aequorea victoria on other species of potentially competing pelagic hydrozoans. *Mar. Ecol. Prog. Ser.* **72**, 255–260 (1991).
15. G. Horridge, The nerves and muscles of medusae. VI. The rhythm. *J. Exp. Biol.* **36**, 72–91 (1959).
16. B. J. Gemmell *et al.*, Passive energy recapture in jellyfish contributes to propulsive advantage over other metazoans. *Proc. Natl. Acad. Sci. U.S.A.* **110**, 17904–17909 (2013).
17. J. O. Dabiri, S. P. Colin, J. H. Costello, Morphological diversity of medusan lineages constrained by animal–fluid interactions. *J. Exp. Biol.* **210**, 1868–1873 (2007).
18. J. O. Dabiri, S. P. Colin, J. H. Costello, M. Gharib, Flow patterns generated by oblate medusan jellyfish: Field measurements and laboratory analyses. *J. Exp. Biol.* **208**, 1257–1265 (2005).
19. S. P. Colin, J. H. Costello, Morphology, swimming performance and propulsive mode of six co-occurring hydromedusae. *J. Exp. Biol.* **205**, 427–437 (2002).
20. B. J. Gemmell, J. H. Costello, S. P. Colin, Exploring vortex enhancement and manipulation mechanisms in jellyfish that contributes to energetically efficient propulsion. *Commun. Integr. Biol.* **7**, e29014 (2014).
21. B. J. Gemmell, D. R. Troolin, J. H. Costello, S. P. Colin, R. A. Satterlie, Control of vortex rings for manoeuvrability. *J. R. Soc. Interface* **12**, 20150389 (2015).
22. L. Passano, Pacemakers and activity patterns in medusae: Homage to Romanes. *Am. Zool.* **5**, 465–481 (1965).
23. M. N. Arai, *A Functional Biology of Scyphozoa* (Springer Science & Business Media, 1997).
24. P. A. Anderson, W. E. Schwab, The organization and structure of nerve and muscle in the jellyfish Cyanea capillata (coelenterata; scyphozoa). *J. Morphol.* **170**, 383–399 (1981).
25. P. A. Anderson, W. E. Schwab, Action potential in neurons of motor nerve net of Cyanea (Coelenterata). *J. Neurophysiol.* **50**, 671–683 (1983).
26. P. A. Anderson, Physiology of a bidirectional, excitatory, chemical synapse. *J. Neurophysiol.* **53**, 821–835 (1985).
27. F. Pallasdies, S. Goedeke, W. Braun, R. M. Memmesheimer, From single neurons to behavior in the jellyfish Aurelia aurita. *Elife* **8**, e50084 (2019).
28. M. E. Demont, J. M. Gosline, Mechanics of jet propulsion in the hydromedusan jellyfish, Polyorchis Pexicillatus: III. A natural resonating bell; the presence and importance of a resonant phenomenon in the locomotor structure. *J. Exp. Biol.* **134**, 347–361 (1988).
29. W. M. Megill, J. M. Gosline, R. W. Blake, The modulus of elasticity of fibrillin-containing elastic fibres in the mesoglea of the hydromedusa Polyorchis penicillatus. *J. Exp. Biol.* **208**, 3819–3834 (2005).
30. B. K. Ahlborn, R. W. Blake, W. M. Megill, Frequency tuning in animal locomotion. *Zoology* **109**, 43–53 (2006).
31. A. Hoover, L. Miller, A numerical study of the benefits of driving jellyfish bells at their natural frequency. *J. Theor. Biol.* **374**, 13–25 (2015).
32. A. P. Hoover, A. J. Porras, L. A. Miller, Pump or coast: The role of resonance and passive energy recapture in medusan swimming performance. *J. Fluid Mech.* **863**, 1031–1061 (2019).
33. R Courant, D. Hilbert, *Methods of Mathematical Physics: Partial Differential Equations* (John Wiley & Sons, 2008).
34. S. P. Colin *et al.*, Biomimetic and live medusae reveal the mechanistic advantages of a flexible bell margin. *PloS One* **7**, e48909 (2012).
35. S. J. Park *et al.*, Phototactic guidance of a tissue-engineered soft-robotic ray. *Science* **353**, 158–162 (2016).
36. C. Christianson, N. N. Goldberg, D. D. Deheyn, S. Cai, M. T. Tolley, Translucent soft robots driven by frameless fluid electrode dielectric elastomer actuators. *Sci. Rob.* **3**, eaat1893 (2018).
37. P. Polygerinos *et al.*, Soft robotics: Review of fluid-driven intrinsically soft devices; manufacturing, sensing, control, and applications in human-robot interaction. *Adv. Eng. Mater.* **19**, 1700016 (2017).
38. J. C. Nawroth *et al.*, A tissue-engineered jellyfish with biomimetic propulsion. *Nat. Biotechnol.* **30**, 792–797 (2012).
39. J. C. Nawroth, K. K. Parker, Design standards for engineered tissues. *Biotechnol. Adv.* **31**, 632–637 (2013).
40. B. E. Griffith, R. D. Hornung, D. M. McQueen, C. S. Peskin, An adaptive, formally second order accurate version of the immersed boundary method. *J. Comput. Phys.* **223**, 10–49 (2007).
41. B. E. Griffith, On the volume conservation of the immersed boundary method. *Commun. Comput. Phys.* **12**, 401–432 (2012).
42. B. Griffith, X. Luo, Hybrid finite difference/finite element immersed boundary method. *Internat. J. Numer. Methods Biomed. Eng.* **33**, e2888 (2017).
43. A. Santhanakrishnan *et al.*, Flow structure and force generation on flapping wings at low Reynolds numbers relevant to the flight of tiny insects. *Fluids* **3**, 45 (2018).
44. W. Kou, B. E. Griffith, J. E. Pandolfino, P. J. Kahrilas, N. A. Patankar, A continuum mechanics-based musculo-mechanical model for esophageal transport. *J. Comput. Phys.* **348**, 433–459 (2017).
45. H. Gao, H. Wang, C. Berry, X. Luo, B. E. Griffith, Quasi-static image-based immersed boundary-finite element model of left ventricle under diastolic loading. *Internat. J. Num. Methods Biomed. Eng.* **30**, 1199–1222 (2014).
46. E. D. Tytell, C. Y. Hsu, T. L. Williams, A. H. Cohen, L. J. Fauci, Interactions between internal forces, body stiffness, and fluid environment in a neuromechanical model of lamprey swimming. *Proc. Natl. Acad. Sci. U.S.A.* **107**, 19832–19837 (2010).
47. A. P. Hoover, B. E. Griffith, L. A. Miller, Quantifying performance in the medusan mechanospace with an actively swimming three-dimensional jellyfish model. *J. Fluid Mech.* **813**, 1112–1155 (2017).
48. G. J. Romanes, *Jelly-fish, Star-fish, and Sea Urchins: Being a Research on Primitive Nervous Systems* (K. Paul, Trench & Company, 1885).
49. G. Horridge, The nerves and muscles of medusae. V. Double innervation in Scyphozoa. *J. Exp. Biol.* **33**, 366–383 (1956).
50. B. J. Gemmell, S. P. Colin, J. H. Costello, J. O. Dabiri, Suction-based propulsion as a basis for efficient animal swimming. *Nat. Commun.* **6**, 8790. (2015).
51. J. O. Dabiri *et al.*, Jellyfish and fish solve the challenges of turning dynamics similarly to achieve high maneuverability. *Fluids* **5**, 106 (2020).
52. W. Gladfelter, Structure and function of the locomotory system of the Scyphomedusa Cyanea capillata. *Mar. Biol.* **14**, 150–160 (1972).
53. A. P. S. Bhalla, B. E. Griffith, N. A. Patankar, A forced damped oscillation framework for undulatory swimming provides new insights into how propulsion arises in active and passive swimming. *PLoS Comput. Biol.* **9**, e1003097 (2013).
54. P. Polygerinos *et al.*, Soft robotics: Review of fluid-driven intrinsically soft devices; manufacturing, sensing, control, and applications in human-robot interaction. *Adv. Eng. Mater.* **19**, 1700016 (2017).
55. W. S. Chu *et al.*, Review of biomimetic underwater robots using smart actuators. *Int. J. Precis. Eng. Manuf.* **13**, 1281–1292 (2012).
56. S. W. Yeom, I. K. Oh, A biomimetic jellyfish robot based on ionic polymer metal composite actuators. *Smart Mater. Struct.* **18**, 085002 (2009).
57. H. Godaba, J. Li, Y. Wang, J. Zhu, A soft jellyfish robot driven by a dielectric elastomer actuator. *IEEE Rob. Autom. Lett.* **1**, 624–631 (2016).
58. C. S. Peskin, The immersed boundary method. *Acta Numer.* **11**, 479–517 (2002).
59. IBAMR, IBAMR: An adaptive and distributed-memory parallel implementation of the immersed boundary method (2020). https://ibamr.github.io/.
60. C. Gambini, B. Abou, A. Ponton, A. J. Cornelissen, Micro- and macrorheology of jellyfish extracellular matrix. *Biophys. J.* **102**, 1–9 (2012).
61. N. W. Xu, J. O. Dabiri, Low-power microelectronics embedded in live jellyfish enhance propulsion. *Sci. Adv.* **6**, eaaz3194 (2020).